machines

MDPI

Article

Demagnetization Analysis and Optimization of Bonded Nd-Fe-B Magnet Rings in Brushless DC Motors

Yinan Wang [1], Hao Zhan [1], Yanyan Gong [1], Mingxu Wang [1,2], Juntao Yu [1,2,3,*], Ze Zhang [4], Yuanfei Yang [4] and Li Wang [1,5,6]

[1] School of Mechanical, Electrical & Information Engineering, Shandong University, Weihai 264209, China
[2] Shandong Key Laboratory of Rare Earth Magnetic Materials and Power Devices, Weihai 264209, China
[3] Preparation and Application of Aerospace High-Performance Composite Materials, Future Industry Laboratory of Higher Education Institutions in Shandong Province, Shandong University, Weihai 264209, China
[4] GRIREM Advanced Materials Co., Ltd., Beijing 100088, China
[5] School of Electromechanical and Automotive Engineering, Yantai University, Yantai 264005, China
[6] Weihai Institute of Industrial Technology, Shandong University, Weihai 264209, China
* Correspondence: juntaoyu@sdu.edu.cn

Abstract: Bonded Nd-Fe-B magnets have greater freedom of shape than sintered Nd-Fe-B magnets. The ring structure is one of the typical structures of bonded Nd-Fe-B materials. In this paper, we analyzed the generation and spread of demagnetization fault (DMF) and changes in motor performance. Meanwhile, a BLDC fitted with a bonded Nd-Fe-B magnet ring was analyzed for DMF under actual overload conditions. DMF occurred with obvious localization and variability, which was mainly concentrated on the side of each pole opposite to the direction of the motor's operation, near the weak magnetic zones. The experimental results show that back electromotive force (EMF) and its harmonic had the same variation trends as the surface radial flux density of the magnet ring. The analysis with the EMF waveform and total harmonic distortion (THD) were proposed as a method for diagnosing the DMF. Finally, this paper presents a modified magnet ring. The anti-demagnetization capability of the modified magnet ring is effectively improved. This research can provide a reference for the design analysis of BLDCs using bonded Nd-Fe-B magnet rings.

Keywords: bonded Nd-Fe-B; demagnetization; finite element analysis; motor; magnet ring

check for updates

Received: 19 December 2024
Revised: 17 January 2025
Accepted: 20 January 2025
Published: 22 January 2025

Citation: Wang, Y.; Zhan, H.; Gong, Y.; Wang, M.; Yu, J.; Zhang, Z.; Yang, Y.; Wang, L. Demagnetization Analysis and Optimization of Bonded Nd-Fe-B Magnet Rings in Brushless DC Motors. *Machines* **2025**, *13*, 75. https://doi.org/10.3390/machines13020075

Copyright: © 2025 by the authors. Licensee MDPI, Basel, Switzerland. This article is an open access article distributed under the terms and conditions of the Creative Commons Attribution (CC BY) license (https://creativecommons.org/licenses/by/4.0/).

1. Introduction

It is well known that brushless DC motors (BLDCs) using Nd-Fe-B magnets as the excitation source have a simple structure and higher torque, power density, and efficiency compared to conventional electrically excited motors [1]. However, the magnetic properties of Nd-Fe-B permanent material are highly susceptible to irreversible demagnetization by temperature and external magnetic fields, which can seriously affect the normal operation of the motor [2,3]. Researchers from industry and academia have investigated demagnetization fault (DMF) [4–7]. Some studies were carried out based on FEM analysis. Qi et al. developed a 2D FEM of a surface-mounted Permanent Magnet Synchronous Motor (PMSM) [8], and, considering the actual conditions and parameters of the motor, verified the DMF resistance of the motor and the feasibility of the finite element simulation. Furthermore, the authors considered the effect of temperature on DMF. The vicious cycle between magnetic performance degradation and temperature rise can exacerbate the DMF [9,10]. Kobayashi et al. modeled a permanent magnet assisted synchronous reluctance motor

(PMASynRM) with embedded bonded NdFeB permanent magnets and analyzed the effect of the relative recoil permeability on its DMF characteristics. The results show that there is no problem in determining the relative recoil permeability to a fixed value for the DMF analysis [11]. Shi et al. established an accurate motor DMF model to determine motor performance under various DMF modes [12]. The correspondence between the DMF amount and the characteristic quantity was established to support the subsequent DMF diagnosis. Some researchers use the characteristics of the motor after demagnetization as a basis for demagnetization diagnosis [13–16]. In [17], Manel et al. used the harmonic analysis of currents to distinguish and describe DMF phenomena. The results concluded that the local DMF introduces specific subharmonics, while uniform DMF leads to an increase in the amplitude of the current at a certain torque. Meanwhile, I. Takeo et al. found that the amplitude of certain frequencies of vibration is approximately proportional to the DMF level of the permanent magnet and the load torque [18], so that the DMF of a PMSM can be evaluated by vibration and torque measurements.

In contrast to the surface-mounted or embedded sintered Nd-Fe-B magnets in the above study, the ring magnets manufactured by the pressing process using bonded Nd-Fe-B material have diverse magnetization methods and are widely used in high-speed micromotors [19,20]. The position of incomplete magnetization exists in the bonded magnet rings, which does not exist in surface-mounted and embedded magnets. The coercivity and remanent magnetism in this position are lower than in the complete magnetization region. Most existing studies do not consider the effect of incompletely magnetized regions in the magnet ring. Therefore, the demagnetization of the bonded magnet ring needs to be further analyzed.

In this paper, we first performed a comparison of different demagnetization models. Then, we modeled a brushless DC motor (BLDC) using a bonded magnet ring. The DMF of the magnet ring under overload was analyzed by considering the high temperature. The operating state parameters of the motor were analyzed using the obtained demagnetization model. Then, we used a prototype to test and characterize the demagnetization of the magnet ring under overload, while the experimental results were compared with the finite element analysis results. We detect the DMF of the magnet rings by testing the back EMF waveform and its total harmonic distortion (THD). Finally, we propose a magnet ring model with a modified inner diameter, and the structure can effectively improve the anti-demagnetization capability of bonded magnetic rings.

2. Comparison of Different Demagnetization Models

The DMF level of the magnet is characterized below using the demagnetization rate (Demag), which is expressed as follows:

$$Demag(\%) = (B_r - B_{r0})/B_r \times 100\% \quad (1)$$

where *Demag* (%) denotes the magnet demagnetization rate, B_{r} denotes the initial remanence of the fully magnetized magnet at that temperature, and B_{r0} denotes the remanence of the magnet after reversion.

As shown in Figure 1a, when the permanent magnet is in normal operation, the working point is located at point (X_1), and the residual magnetic induction of the magnet can return to the normal remanence in B_{r} along the demagnetization curve. When the load increases, the winding current increases, and the working point moves from X_1 to point X_2 along the demagnetization curve. If the motor stops at this point, the remanence of the magnet will not return to B_{r}, but instead reach the position of B_{r1} along the new return line (dashed line). The irreversible demagnetization happens in the permanent magnet. In the actual working condition, overload will increase the temperature (T),

which is especially obvious in high-speed micro-motors. Hence, the effect of temperature needs to be considered when the demagnetization analysis is performed. Figure 1b shows the demagnetization analysis model of the motor at different temperatures. When the temperature rises from T_1 to T_2, the working point moves from X_3 to X_4, and the residual magnetic induction will reach B_{r2} from X_4 along the new recoil line.

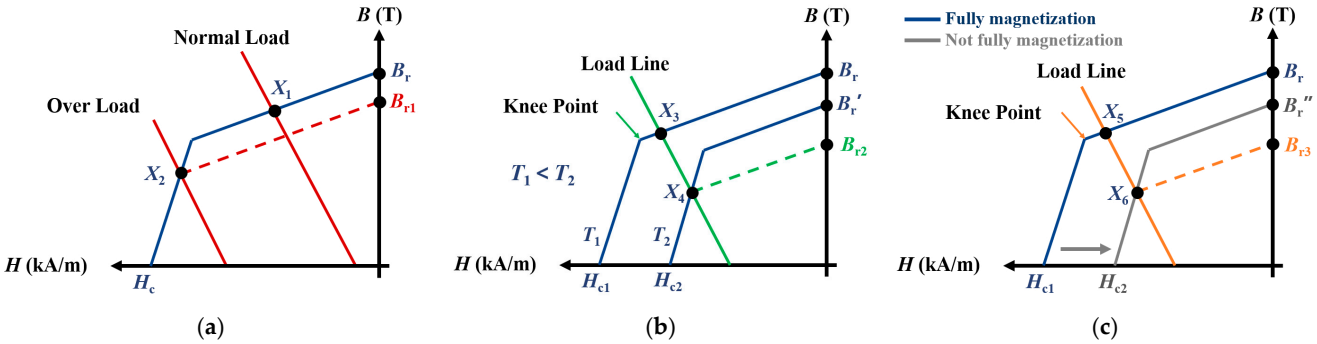


Figure 1. Irreversible demagnetization: (**a**) disregarding temperature; (**b**) considering temperature; (**c**) different magnetization positions.

The variability in demagnetization at different magnetization positions is also worth investigating. As shown in Figure 1c, the higher region of magnetization corresponds to the remanence B_r and coercivity H_{c1}, while the lower region corresponds to the remanence $B_{r'}$" and coercivity H_{c2}. When subject to the same demagnetization field, the working point of the strong magnetic zone is located at X_5, above the knee point where no DMF occurs. However, the weak magnetic zone is located at X_6, below the knee point of the demagnetization curve, and the remanent magnetization of the transition zone after the return is B_{r3}, and irreversible demagnetization occurs.

3. Motor Parameters and FEM Analysis Settings

3.1. Subsection Motor Structure

A six-slot four-pole BLDC was used for the FEM analysis. The motor has an internal rotor structure, and its main parameters are shown in Table 1. The motor's structure is shown in Figure 2. The axis of the N-pole of the rotor is aligned with the U-phase axis in the initial position. The rotor running direction is counterclockwise. This brushless DC motor uses an inverter control circuit, as shown in Figure 3.

Table 1. Specifications of the motor model.

Main Parameters	Value	Main Parameters	Value
Rated power	100 W	Rotor core	S45C
Number of slots	6	Rated speed	5000 rpm
Number of poles	4	Turns per slot	120
Out diameter	55 mm	Rated temperature	60 °C
Axial length	22 mm	Permanent magnet	GBM-8
Phase number	3	Outer diameter of the magnet	26 mm
Air gap width	0.3 mm	Inner diameter of the magnet	18 mm
Stator core	35JN230	Axis height of the magnet	20 mm

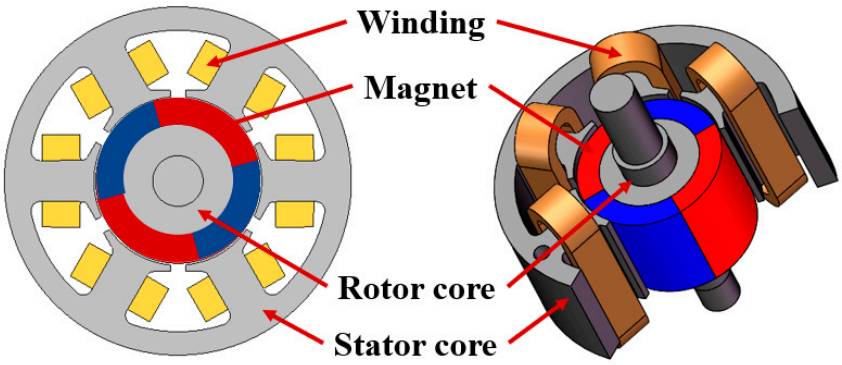


Figure 2. Schematic of the experimental motor using a bonded magnet ring.

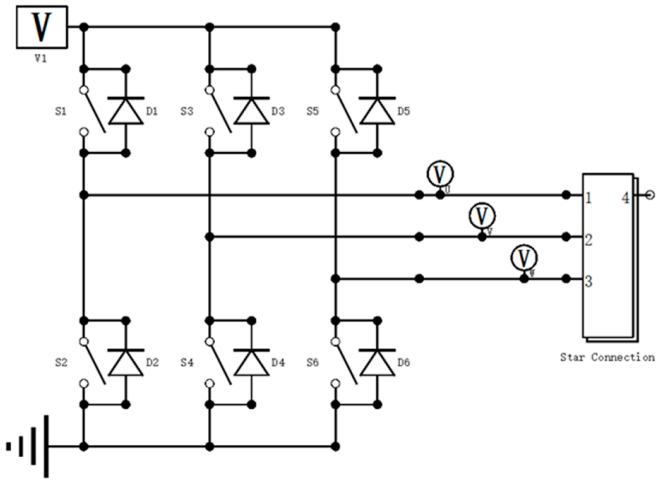


Figure 3. Voltage source inverter circuit.

Since the actual motor structure is more complex, this paper uses a simplified and idealized motor model for FEM analysis. In the simplification and idealization process, the following assumptions are made: (1) The temperature effects of magnetic permeability and electrical conductivity are ignored. (2) The Z-axis component of the magnetic flux is neglected. (3) The effect of the displacement current on the electromagnetic field is neglected. (4) The material is assumed to be isotropic, ignoring the hysteresis effect of the ferromagnetic material. (5) The eddy current effect of the stator–rotor core and source current position are not considered. The time-step FEM method is used for electromagnetic field analysis.

3.2. Magnetization Method of the Magnet Ring

The motor uses a bonded Nd-Fe-B magnet ring. The bonded PM has a radial four-pole magnetization, and the magnetization waveform is trapezoidal, as shown in Figure 4. The single pole cross-section of the four-pole ring is shown in Figure 5, with a width of 90 deg. It can be divided into three areas: the BC (θ_2) area with a width of 75 deg, which is charged to magnetic energy saturation, called the main magnetic area; and AB (θ_1) and CD (θ_3), which are the transition areas between the poles, with pole widths of 7.5 deg. In these areas, the magnets are not magnetized to saturation, and are called the weak magnetic zones.

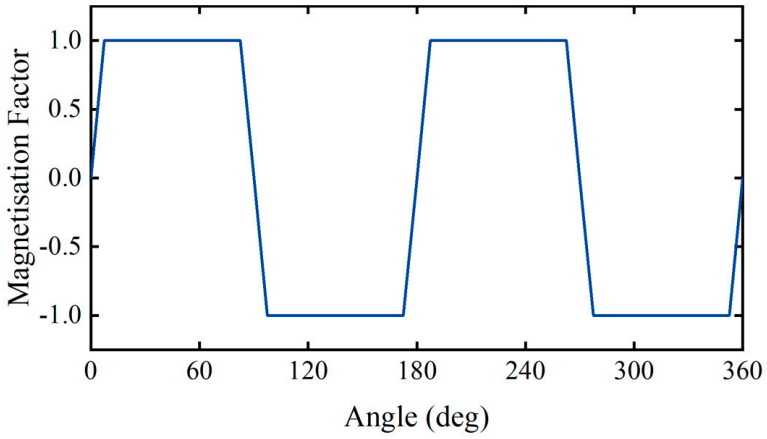


Figure 4. Magnetization rate for magnet rings (normalization).

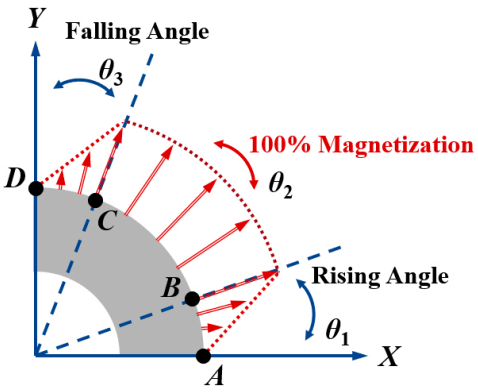


Figure 5. Schematic diagram of single pole magnetization.

4. Discussion of FEM Analysis Results

Under normal conditions, irreversible demagnetization will not occur. To analyze the DMF of the bonded Nd-Fe-B magnet ring under severe operating conditions, we assume that the rotor magnet ring has a uniform temperature distribution and that the motor has been operating under rated conditions for a period. When the motor is at rated operating temperature (60 °C), it was subjected to 1.5 times load and double load, causing the motor temperature to rise to the designed maximum operating temperature of 130 °C in a short time. Under these conditions, an irreversible demagnetization model of the motor was obtained.

4.1. Demagnetization of the Magnet Ring

The cloud of the magnetic flux density distribution for different cases of the motor, combining the effects of temperature and armature response, is shown in Figure 6. At the same FEM time-step, an increase in load leads to an increased armature reaction effect and a significant local reduction in the flux density of the magnet occur. The cloud plot of the DMF rate distribution of permanent magnets calculated according to Equation (1) is shown in Figure 7. The arrow in the Figure 7 indicates the direction of motor rotation. There are four weak magnetic zones with low magnetic flux density between the main magnetic poles, as shown in the dotted line position. According to the DMF rate calculation method, the demagnetization of these four weak magnetic zones is at a high level in the initial state. This is unavoidable in the multi-pole ring magnetization process.

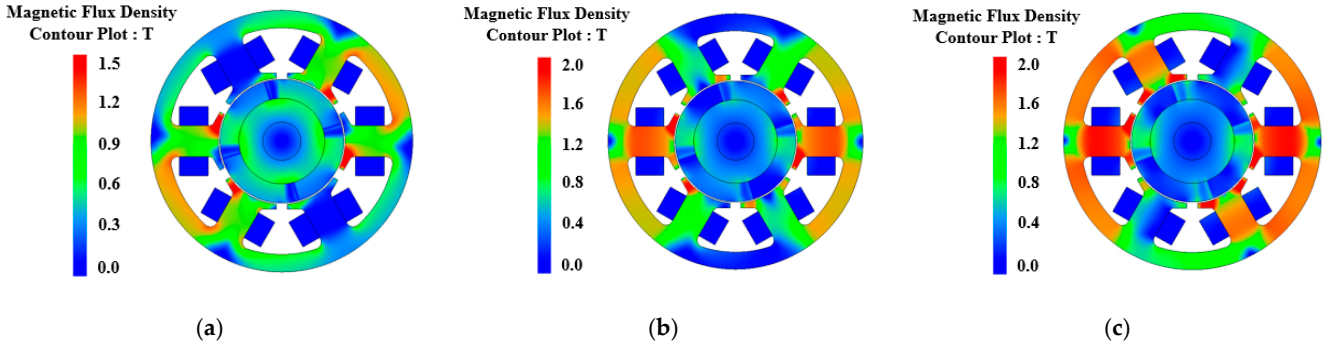


Figure 6. Flux maps of motor magnetic flux density for different load cases: (**a**) normal load, (**b**) 1.5 times load, (**c**) double load.

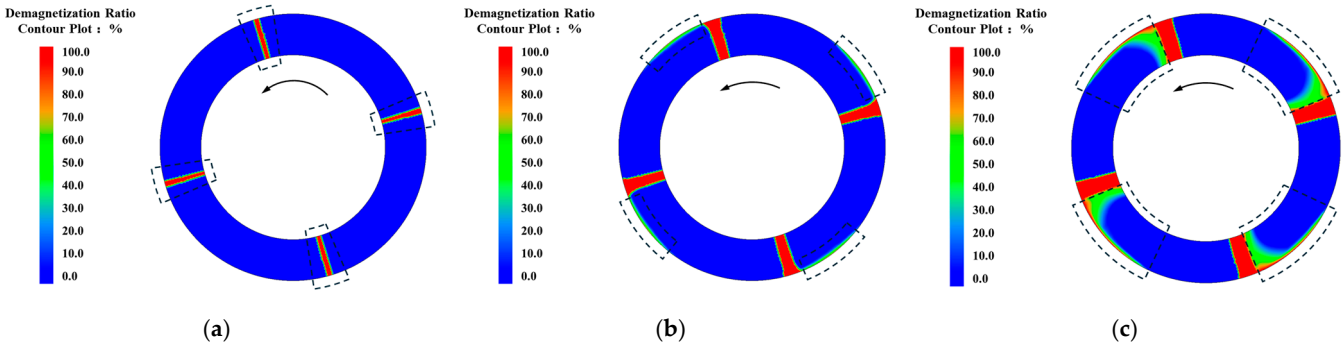


Figure 7. Demagnetization ratio maps in different load cases: (**a**) normal load, (**b**) 1.5 times load, (**c**) double load.

When in the 1.5 times overload case, the DMF distribution of the magnetic ring changes in two ways. First, the position of the transition region between the magnetic poles is more severely demagnetized, and the entire transition region becomes wider. At the same time, additional DMF areas appear on the outer surface of the magnetic ring near the transition area. The same DMF occurred in each of the four poles of the magnetic ring. This is because the motor does not break in time after an overload, and the temperature rise and armature response can remain for several mechanical cycles, with each pole being affected. It is worth noting that DMF occurs in a regular pattern, and the newly added DMF is concentrated on the side of each magnetic pole opposite the direction of motor operation. Combining the theory of motor control, under load conditions, the winding magnetic field has a magnetizing effect on the first half of a single magnetic pole and a demagnetizing effect on the second half.

When a double overload is applied, the DMF area is further extended. The DMF on the outer surface of the ring increases, while the DMF spreads along the radial direction of the ring towards the inner surface. This phenomenon is particularly serious near transitional zones. The lower coercivity of the weak magnetic zones is one of the reasons for the more severe radial spread of demagnetization.

4.2. Effect of Demagnetization on Motor Parameters

The demagnetized motor model was used for analyzing the surface radial magnetic flux density (B_s) and back EMF. Figure 8 shows the B_s for the normal case compared to the DMF case. When the overload causes partial demagnetization of the permanent magnet, the B_s and the EMF also decrease locally in the figure, presenting a local distribution consistent with the demagnetization case above. We use the magnetic flux area to measure the change in magnetic properties of the magnetic ring. The magnetic flux area is the area enclosed by

the magnetic flux waveform and the angular coordinates of each magnetic pole. The unit is T·deg (Tesla × angle). The physical meaning is expressed as the integral of the magnetic flux response with respect to the angle. The magnetic area of a normal magnetic ring is 14.52 T·deg and reduced to 13.70 T·deg after 1.5 times overload. After double overload, the magnetic area is reduced to 12.37 T·deg. Magnetic area decreased by 14.81%.

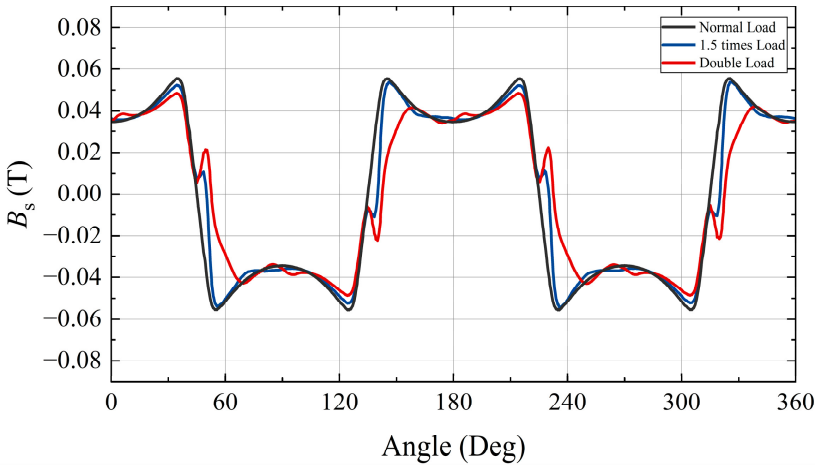


Figure 8. Comparison of B_s after DMF with different loads.

Fourier transform (FFT) analysis was performed on the B_s. From Figure 9, it can be observed that the main harmonics of B_s are odd orders such as 3, 5, and 7. The fundamental, third, and fifth harmonics amplitudes decrease as the DMF worsens. We calculated the total harmonic distortion (THD) using Equation (2).

$$THD = \sqrt{\sum_{n=2}^{H} \left(\frac{G_n}{G_1} \right)^2} \tag{2}$$

where H is the highest harmonic order, n is the harmonic order, G_n is the nth harmonic amplitude, and G_1 is the fundamental wave amplitude. As Table 2 shows, the THD of the B_s in the normal load case is 54.9%, in the 1.5 times case is 46.7%, and in the double load case is 31.7%. It was found that as the DMF increases, the harmonic distortion of the surface magnetization shows a decreasing trend.

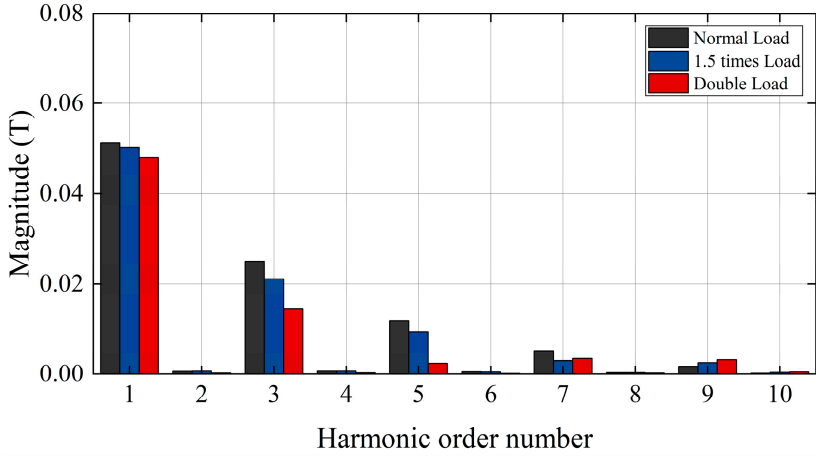


Figure 9. Harmonic comparison of B_s in different DMF cases.

Table 2. Surface radial magnetic flux density harmonic analysis in different DMF cases.

Harmonic Order Number	Normal Load (T)	1.5 Times Load (T)	Double Load (T)
1	0.05141	0.05024	0.04801
2	6.30369×10^{-4}	6.45125×10^{-4}	2.54166×10^{-4}
3	0.025	0.02113	0.01428
4	6.45558×10^{-4}	6.86865×10^{-4}	2.68177×10^{-4}
5	0.01182	0.00934	0.00241
6	5.01838×10^{-4}	4.88926×10^{-4}	1.27954×10^{-4}
7	0.00518	0.00298	0.00345
8	3.27925×10^{-4}	3.41862×10^{-4}	2.15618×10^{-4}
9	0.00175	0.00258	0.00319
10	2.13082×10^{-4}	3.62442×10^{-4}	4.97643×10^{-4}
THD	54.9%	46.7%	31.7%

Figure 10 shows a comparison of the back EMF waveforms after demagnetization. At the location where demagnetization occurs, the generated back EMF value will decrease. Therefore, the pattern of the back-EMF waveform is similar to that of the magnetic waveform, which is characterized by a significant decrease on one side. The main harmonic of the back EMF, shown in Figure 11, is the fifth harmonic, and as the demagnetization increases, the amplitudes of the fundamental wave and the fifth harmonic decrease. In Table 3, the THD of the back EMF in the normal load case is 12.5%, in the 1.5 times load case is 10.0%, and in the double load case is 4.2%. From the results of the harmonic analysis, for bonded magnetic rings magnetized with a trapezoidal wave, as the DMF develops and worsens, the harmonic distortion rates of both Bs and the back EMF decrease.

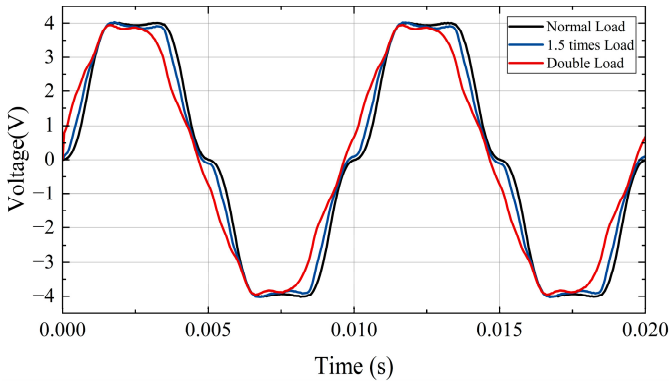


Figure 10. Waveform comparison of back EMF after DMF in different loads.

Table 3. No-load back EMF harmonic analysis in different DMF cases.

Harmonic Order Number	Normal Load (V)	1.5 Times Load (V)	Double Load (V)
1	4.29901	4.21445	4.05471
2	0.03508	0.03467	0.02036
3	0.01529	0.01488	0.01205
4	0.02723	0.0265	0.01459
5	0.50472	0.40665	0.13395
6	8.33972×10^{-4}	0.00139	0.00567
7	0.17315	0.10044	0.09681
8	0.00679	0.00416	0.00565
9	0.0015	0.00154	0.00566
10	0.0022	0.00575	0.01002
THD	12.5%	10.0%	4.2%

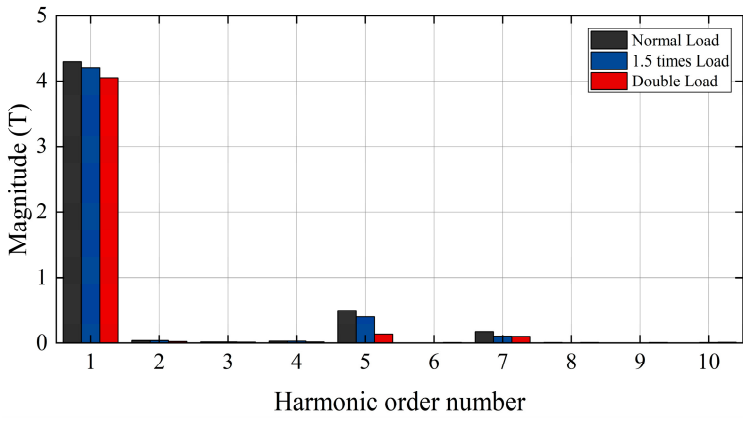
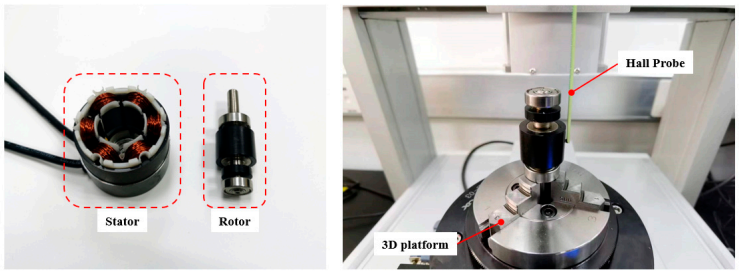


Figure 11. Harmonic comparison of back EMF for different DMF cases.

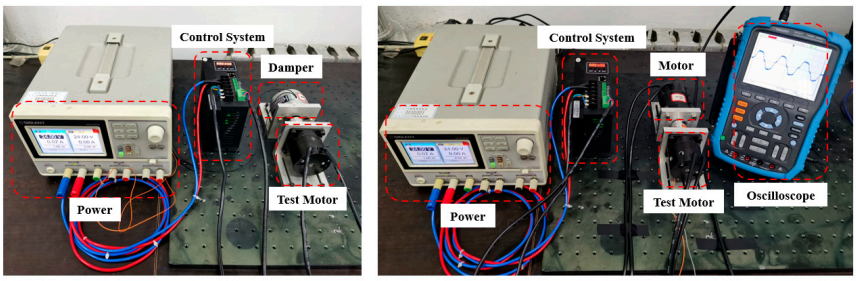
5. Experimental Analysis

The experiments were designed using a BLDC equipped with a bonded Nd-Fe-B magnet ring (Grirem Advanced Materials, Beijing, China), as shown in Figure 12a, which was magnetized in the same way as in the FEM analysis. Figure 13a shows the schematic diagram of the load test, and the motor is a selected closed-loop control. To simulate actual overloading and avoid motor damage, the hysteresis damper (HaiBoHua, Beijing, China) was controlled using the computer program, and the intermittent pulse loads are applied to the motor to simulate the effect of motor overload. Each load application time was not less than one mechanical cycle. We measured the B_s using a high-precision Tesla probe (Forever Elegance Technology, Loudi City, China), which is shown in Figure 12b. The DMF diagnosis is performed by measuring the single-phase back EMF of the motor in Figure 13b.



(**a**) (**b**)

Figure 12. Experiment protype: (**a**) test motor, (**b**) magnet ring rotor.



(**a**) (**b**)

Figure 13. Test platforms: (**a**) load test, (**b**) single-phase back EMF test.

Figure 14a shows the B_s of the original magnet ring. It can be observed that the surface magnetic distribution is not uniform in the main magnetic region of each pole. The Bs is relatively high at both ends of the main magnetic zone, as the ends are more likely to form

magnetic circuit closures with the adjacent poles. The resistance to forming a magnetic circuit closure in the middle of the main magnetic region is relatively high, thus creating a saddle position with relatively low apparent magnetic property. The distribution of the 3D surface flux density also explains why the B_s shows saddle waves in the results of the 2D FEM analysis. The value of Bs between the peak in the main magnetic area and the lowest in the saddle is 16.92%.

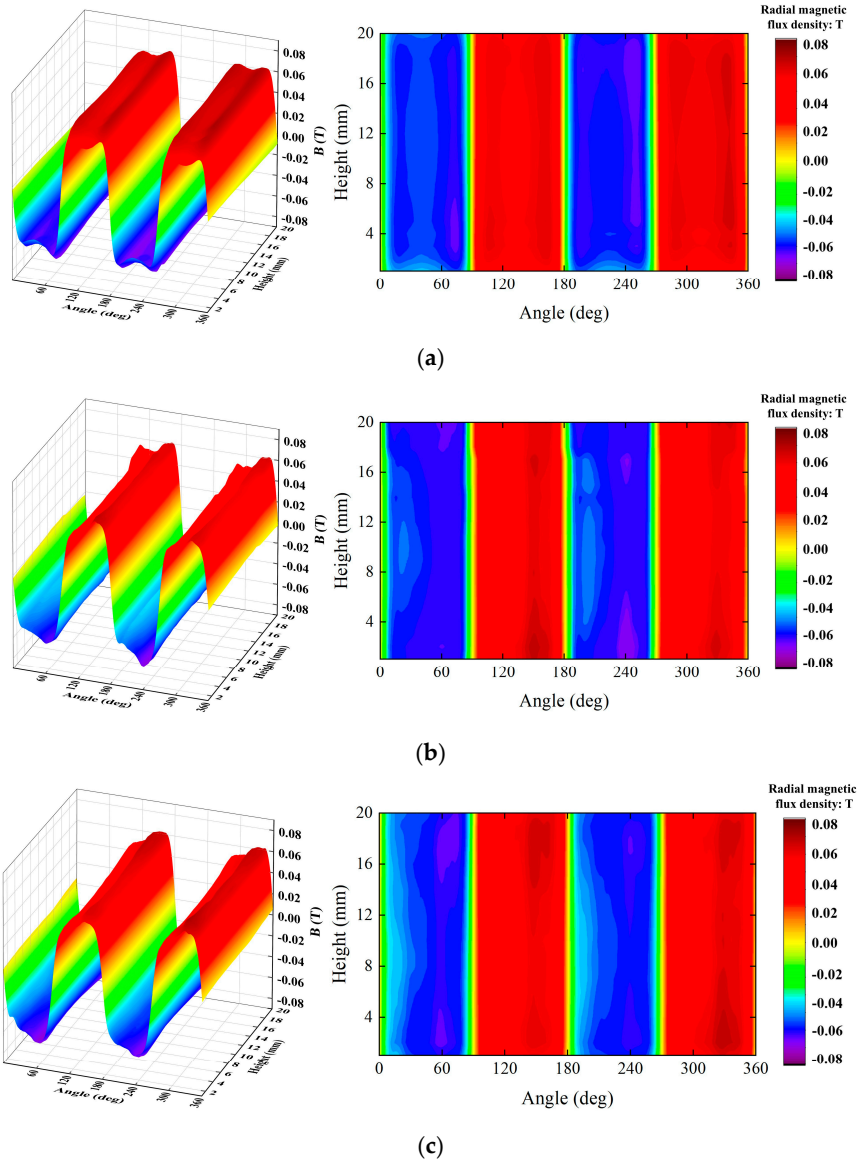


Figure 14. B_s distribution after demagnetization with different loads: (**a**) normal load, (**b**) 1.5 times load, (**c**) double load.

Figure 14b shows the B_s of the magnet ring in the 1.5 times load case. The location of the flux density distribution in the main magnetic zone has changed significantly. The saddle position of the B_s has disappeared. The B_s decreases on the left side opposite to the running direction of the motor. Figure 14c shows the B_s of the magnet ring in the double load case. The variability on either side of the pole increases further. The range in DMF is further extended compared to the Figure 14b case. It can be observed that the DMF is severe near the weak magnetic zones and spreads to the pole center with an increase in the load current, and the lower coercivity and remanent magnetism in the weak magnetic zones is one of the reasons for the above phenomenon.

Figure 15 shows the B_s of the magnet ring at the mid-axial position. Consistent with the FEM analysis shown in Figure 10, the DMF occurs on the left side of the peak position. Therefore, the B_s in the left of each pole in Figure 15 is significantly lower. The magnetic area in the normal case at this location is 16.64 T·deg. The magnetic area is reduced to 15.38 T·deg in the 1.5 times load case and reduces to 14.39 T·deg in the double load case. Due to the overall reduced flux density of the magnet ring, the B_s amplitude on the right side of the poles is also lower than normal ring. Figure 16 shows a harmonic analysis of the B_s. As the DMF increases, the amplitude of both the fundamentals and harmonics decreases.

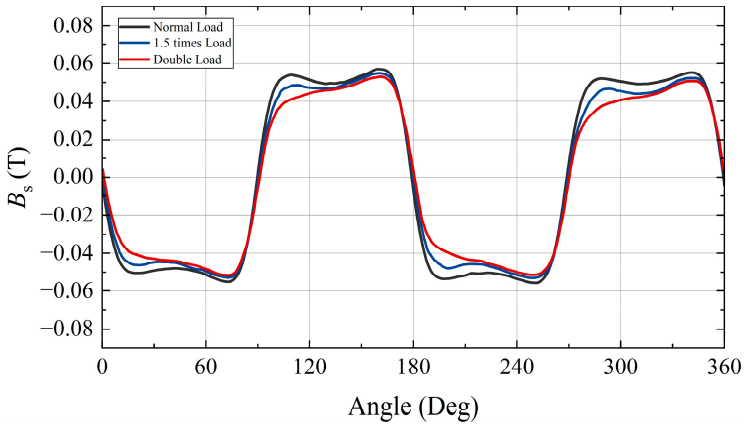


Figure 15. Comparison of B_s at the axial mid-position of the magnet ring.

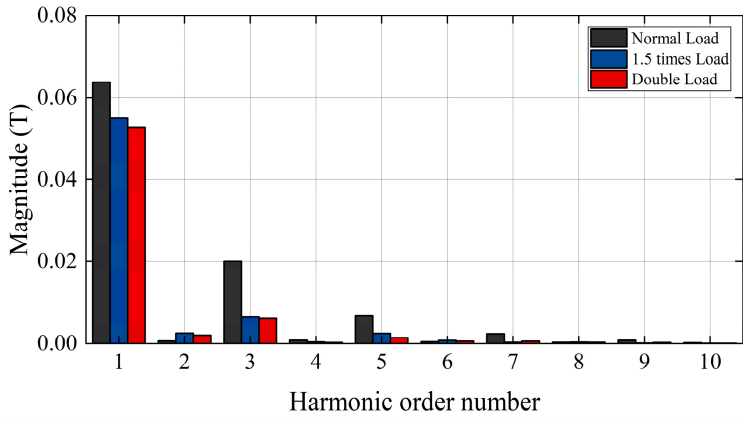


Figure 16. Harmonic analysis of the Bs in the axial mid-position of the magnet ring.

In the FFT analysis of the surface magnetic waveform shown in Table 4, the THD is 33.4% under normal conditions and reduces to 13.5% in the 1.5 times case, a reduction of 19.9%. The THD in double load case is 12.8%, a decrease of 20.6% compared to the normal case. The results show that, for the trapezoidal wave magnetized magnet ring, the THD of Bs decreases as the DMF increases.

A comparison with the FEM results shows that the peak-to-saddle difference for each pole in the FEM results is higher than in the experimental results. This is due to the variability in surface magnetic flux density testing. In the FEM analysis, the software constitutes a curve by collecting the radial flux density component at each node, while in the prototype experiments, the test results of the surface flux density are affected by the spatial resolution of the Hall probe, and the accuracy of the waveform is related to the size of the probe area. As shown in Table 5, there are some numerical differences between the results of the FEM analysis and the experimental analyses. However, the

flux density distribution characteristics and the demagnetization generation and diffusion pattern derived from the FEM analysis are consistent with the experimental results. After partial demagnetization of the magnet ring, the B_s waveform is distorted. The maximum value of B_s, the magnetic area, and the THD are reduced.

Table 4. Harmonic analysis of surface flux density.

Harmonic Order Number	Normal Load (T)	1.5 Times Load (T)	Double Load (T)
1	0.06379	0.05503	0.05261
2	6.45054×10^{-4}	0.00253	0.00205
3	0.01999	0.00646	0.00612
4	8.53194×10^{-4}	4.05759×10^{-4}	3.03526×10^{-4}
5	0.00675	0.00246	0.00149
6	4.67153×10^{-4}	8.00305×10^{-4}	6.28393×10^{-4}
7	0.00239	3.12326×10^{-4}	6.41333×10^{-4}
8	3.23385×10^{-4}	3.88394×10^{-4}	3.56543×10^{-4}
9	8.50724×10^{-4}	1.29257×10^{-4}	2.85682×10^{-4}
10	2.49104×10^{-4}	9.86289×10^{-5}	8.67477×10^{-5}
THD	33.4%	13.5%	12.8%

Table 5. Comparison of FEM and experimental analysis results for Bs.

		FEM Analysis	Experimental
Maximum value of the B_s (mT)	Normal load	55.2	57
	1.5 times load	53.6	54.7
	Double load	48.2	52.8
Magnetic area (T deg)	Normal load	14.52	16.64
	1.5 times load	13.70	15.38
	Double load	12.37	14.39
THD	Normal load	54.9%	33.4%
	1.5 times load	46.7%	13.5%
	Double load	31.7%	12.8%

As shown in Figure 17, the trend in the no-load back EMF is consistent with the trend in the surface magnetic energy. As the overload increases, the amplitudes of both the fundamental wave and the fifth harmonic decrease, which is shown in Figure 18.As Table 6 shows, the THD of back EMF in normal load case is 11.6%, reduces to 11.0% after the 1.5 times case, and decreases to 10.6% in the double case.

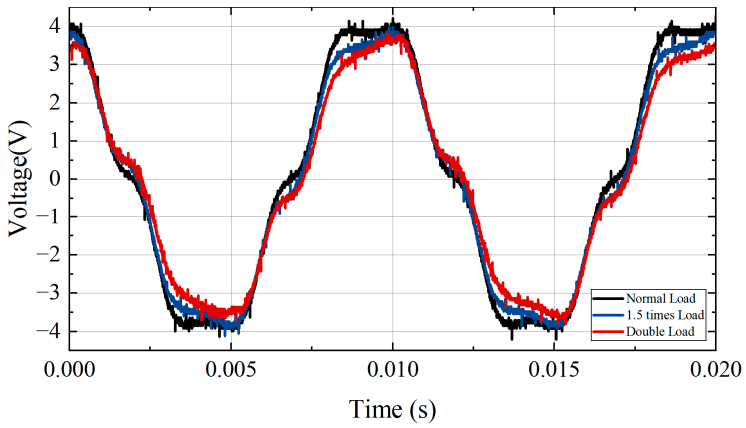


Figure 17. Back EMF after different load tests.

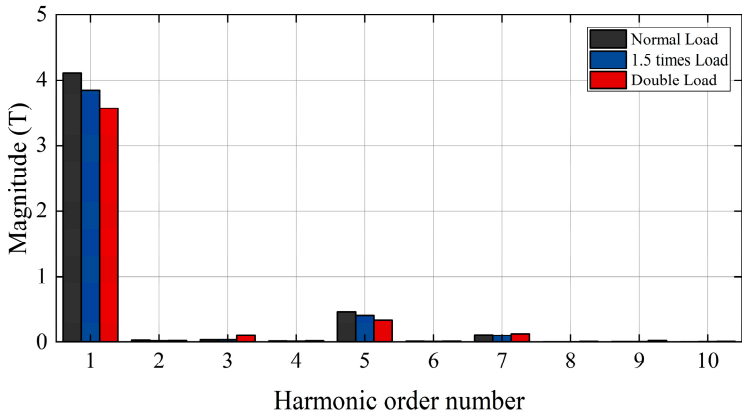


Figure 18. Harmonic analysis of back EMF after different load tests.

Table 6. Harmonic analysis of single-slot back EMF.

Harmonic Order Number	Normal Load (V)	1.5 Times Load (V)	Double Load (V)
1	4.10982	3.84381	3.57322
2	0.02308	0.01466	0.01738
3	0.02913	0.02962	0.1054
4	0.01047	0.00955	0.0157
5	0.46324	0.41052	0.34206
6	0.0075	0.00482	0.00824
7	0.10773	0.09779	0.12488
8	0.00136	7.24171×10^{-4}	0.00494
9	0.00214	0.00151	0.0168
10	0.00133	0.00377	0.00554
THD	11.6%	11.0%	10.6%

As shown in Table 7, the variation trend in the no-load back EMF of the experimental prototype is consistent with the results of the FEM analysis. Following the occurrence of local demagnetization, both the maximum value of the no-load back EMF and the THD decrease. This observation suggests that the waveform variation in the no-load back EMF can serve as an effective real-time indicator of magnet ring demagnetization.

Table 7. Comparison of FEA results and experimental analysis of Bs.

		FEM Analysis	Experimental
Maximum value of the no-load back EMF (V)	Normal load	4.05	4.2
	1.5 times load	4.02	3.98
	Double load	3.95	3.8
THD	Normal load	12.5%	11.6%
	1.5 times load	10.0%	11.0%
	Double load	4.2%	10.6%

6. Anti Demagnetization Optimization

As has been shown above, for the loading working condition of the bonded Nd-Fe-B magnetic ring, the DMF is concentrated around the weak magnetic zones. This paper proposes a magnetic ring inner diameter function that selectively enhances the demagnetization resistance in the transition zone while minimizing the amount of bonded Nd-Fe-B used. The modified inner diameter of the magnetic ring is shown in Figure 19.

The outer diameter D_2 is 26 mm and the inner diameter D_1 is 18 mm. The modified inner diameter D_m satisfies Formula (3).

$$D_{\mathrm{m}} = D_1 + H \times \cos(\mathrm{p} \times \theta) \tag{3}$$

where D_m is the modified inner diameter, D_1 is the inner diameter of the ordinary magnetic ring, H is the adjustment parameter, and p is the number of poles. As shown in Figure 19, the modified inner diameter selectively increases the thickness of the weak magnetic zones between the magnetic poles, while reducing the thickness of the main magnetic pole region to reduce the amount of bonded NdFeB used. The value of H needs to be optimized using the finite element method. An excessively large H value will affect the magnetic properties of the main magnetic pole.

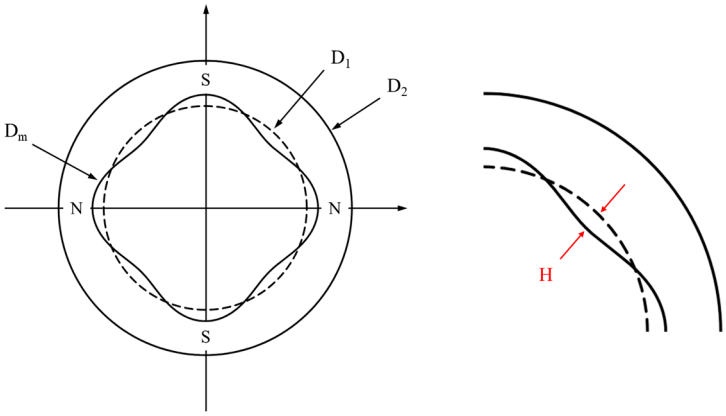


Figure 19. Modified inner diameter magnet ring.

In this paper, we use parametric finite element simulation to determine the optimal value of *H*, which takes the value of 0–1.5 mm. As shown in Figure 20, the magnetic flux area after demagnetization of the magnet ring shows an increasing and then decreasing trend as the variable *H* increases. When *H* = 0.5 mm, the magnetic area after demagnetization of the magnet ring reaches its maximum value. As the parameter *H* increases, the THD of the Bs increases. An increase in harmonic content can lead to an increase in cogging torque, along with problems such as vibration noise. Therefore, we choose *H* = 0.5 mm for our analysis here.

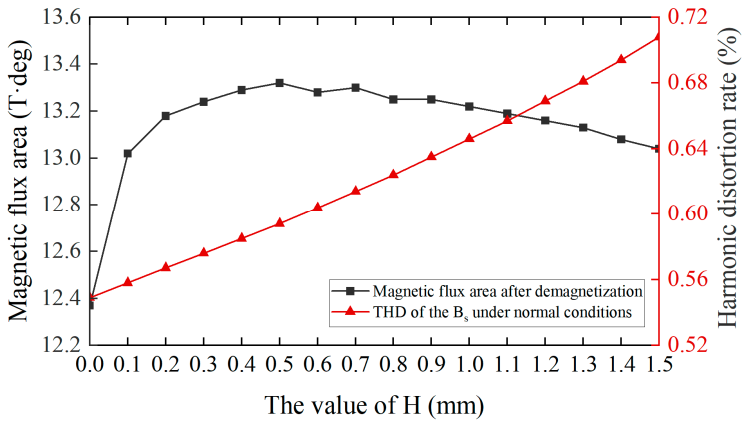
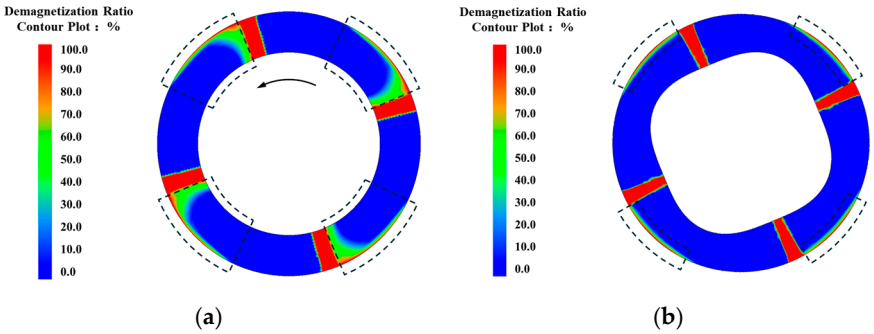


Figure 20. Parametric optimization search for *H* values.

The anti-demagnetization effect of the modified magnet ring is verified by comparing the DMF of the original magnet ring and the modified magnet ring under double overload conditions. As shown in Figure 21, under the same double overload conditions, the

demagnetization area of the modified magnet ring is significantly reduced, and, at the same time, the demagnetization phenomenon spreading from the outer surface to the inner surface near the weak magnetic zone disappears.



(**a**) (**b**)

Figure 21. Comparison of demagnetization results in double load case: (**a**) original magnet ring, (**b**) modified magnet ring.

Figure 22 shows the B_s of the optimized magnetic ring under double overload conditions. The local demagnetization trend caused by the overload is consistent with the previous analysis, mainly concentrated on one side of the magnetic pole, but the degree of demagnetization of the magnet is significantly reduced after optimization. The magnet ring with modified inner diameter has a magnetic area of 14.34 T·deg under normal conditions. After the DMF, the magnetic area is reduced to 13.32 T·deg. Magnetic area decreased by 7.11%, which is a significant improvement compared to the original magnet ring. Figure 23 shows the waveform of the back EMF. A comparison with the FEA results in FEM analysis shows that, under the same working condition of the double overload, the distortion of the back EMF waveform decreases due to the reduction in DMF. Combining the results of the above analysis, the anti-demagnetization capability of the modified magnet ring is significantly improved.

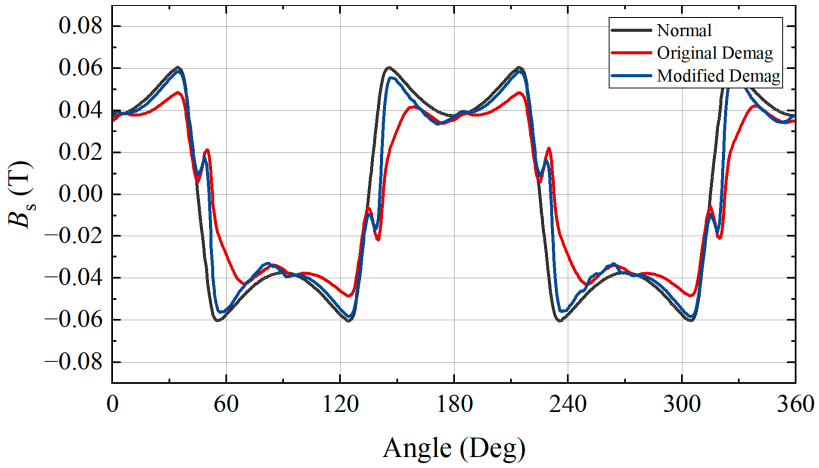


Figure 22. Comparison of B_s after demagnetization of the original and modified magnet ring.

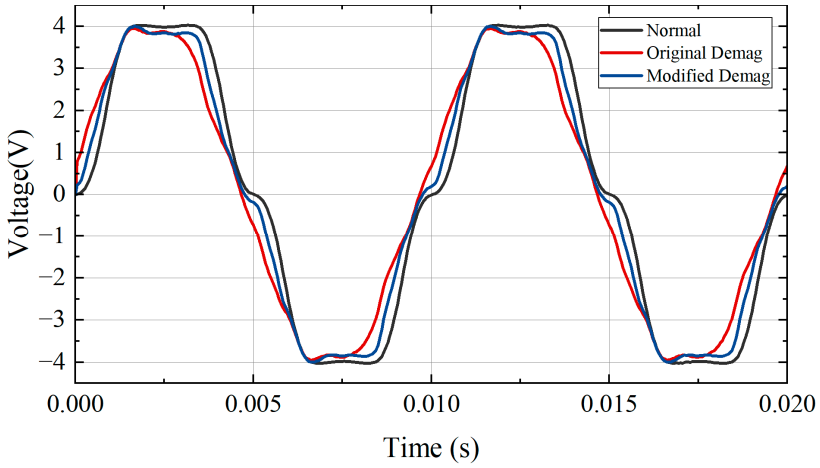


Figure 23. Comparison of back EMF after demagnetization of the original and modified magnet ring.

7. Conclusions

In this paper, the demagnetization of ring-shaped bonded Nd-Fe-B magnets in brushless DC motors is studied using the finite element method and prototype experiments. The magnetic ring structure is optimized to resist demagnetization, with the following conclusions:

(1) When the motor is under overload, the low coercive force and remanence in the transition position between the poles of the ring magnet cause severe irreversible demagnetization in this position. Demagnetization first appears on the outer surface of the magnet ring and spreads radially to the inner surface near the transition position as the demagnetization intensifies. Therefore, improving the anti-demagnetization capability of the weak magnetic region is very effective in avoiding DMF.

(2) The demagnetization of magnets that occurs during overload has local differences, and the location of demagnetization is mainly concentrated on the side of each magnetic pole opposite the direction of motor operation. For a trapezoidal wave magnetizing ring, after local DMF occurs, the harmonic distortion rates of both the surface magnetic flux waveform and the back electromotive force waveform decrease. Therefore, the waveform distortion of the back electromotive force can be used as one of the means to detect demagnetization.

(3) The magnetic ring with a modified inner diameter proposed in this paper selectively enhances the resistance to demagnetization near the transition region, which can effectively reduce the demagnetization rate of the bonded magnetic ring under overload conditions.

Author Contributions: Conceptualization, Y.W. and H.Z.; methodology, Y.W.; software, Y.W.; validation, Y.W., Y.G. and M.W.; formal analysis, Y.W.; investigation, Y.W.; resources, Y.W.; data curation, Z.Z. and Y.Y.; writing—original draft preparation, Y.W. and J.Y.; writing—review and editing, Y.W.; visualization, J.Y.; supervision, L.W.; project administration, L.W.; funding acquisition, L.W. All authors have read and agreed to the published version of the manuscript.

Funding: This research was funded by the National Key Research and Development Program of China (No. 2021YFB3500205), the Key Research and Development Plan of Shandong Province (No. 2022CXGC020307 and No. 2023JMRH0303).

Data Availability Statement: Data are contained within the article.

Conflicts of Interest: Authors Ze Zhang and Yuanfei Yang were employed by the company GRIREM Advanced Materials Co., Ltd. The remaining authors declare that the research was conducted in the absence of any commercial or financial relationships that could be construed as a potential conflict of interest.

References

1. Reigosa, D.; Fernández, D.; Park, Y.; Diez, A.B.; Lee, S.B.; Briz, F. Detection of Demagnetization in Permanent Magnet Synchronous Machines Using Hall-Effect Sensors. *IEEE Trans. Ind. Appl.* **2018**, *54*, 3338–3349. [CrossRef]
2. Usman, A.; Rajpurohit, B.S. Characteristic Analysis of Partial Demagnetization Faults in Surface Mounted BLDC Motors. In Proceedings of the 2020 IEEE Industry Applications Society Annual Meeting, Detroit, MI, USA, 10–16 October 2020; IEEE: New York, NY, USA, 2020.
3. Leem, K.D.; Kim, W.H.; Jin, C.S.; Lee, J. Local demagnetisation analysis of a permanent magnet motor. *IET Electr. Power Appl.* **2015**, *9*, 280–286.
4. Iang, L. Recent Status of Bonded Nd-Fe-B Magnets. *J. Iron Steel Res. Int.* **2006**, *13*, 265–267.
5. Bai, S.X.; Hong, Z.; Li, L.V.; Ke, C.; Cai, H.N. Progress of Research on Bonded Nd-Fe-B Magnets. *J. Iron Steel Res. Int.* **2006**, *13*, 489–493. [CrossRef]
6. Ullah, Z.; Hur, J.A. Comprehensive Review of Winding Short Circuit Fault and Irreversible Demagnetization Fault Detection in PM Type Machines. *Energies* **2018**, *11*, 3309. [CrossRef]
7. Chen, Y.; Liang, S.; Li, W.; Liang, H.; Wang, C. Faults and Diagnosis Methods of Permanent Magnet Synchronous Motors: A Review. *Appl. Sci.* **2019**, *9*, 2116. [CrossRef]
8. Qi, D.; Jing, Y.; Zhang, S. The Study of Permanent Magnet Demagnetization in Permanent Magnet Synchronous Motor. In Proceedings of the 2021 IEEE International Conference on Advances in Electrical Engineering and Computer Applications (AEECA), Dalian, China, 27–28 August 2021.
9. Zhang, W.; Li, G.; Zhu, Z.; Ren, B.; Chong, Y.C.; Michon, M. Demagnetization Analysis of Modular SPM Machine Based on Coupled Electromagnetic-Thermal Modelling. *Energies* **2022**, *16*, 131. [CrossRef]
10. Zhao, P.; Yu, Y.Q. Analysis of Influence of Permanent Magnet Demagnetization on Motor Temperature Rise. *J. Phys. Conf. Ser.* **2022**, *2395*, 012–022. [CrossRef]
11. Kobayashi, M.; Morimoto, S.; Sanada, M.; Inoue, Y. Effect of Variable Recoil Permeability on Demagnetization Characteristics of Permanent Magnet Assisted Synchronous Reluctance Motor with Bonded Magnets. *IEEJ J. Ind. Appl.* **2021**, *10*, 675–681. [CrossRef]
12. Shi, C.; Peng, L.; Zhang, Z.; Shi, T. Analytical Modeling and Analysis of Permanent-Magnet Motor with Demagnetization Fault. *Sensors* **2022**, *22*, 9440. [CrossRef] [PubMed]
13. Isermann, R. Model-based fault-detection and diagnosis—Status and applications. *Annu. Rev. Control* **2005**, *29*, 71–85. [CrossRef]
14. Bellini, A.; Filippetti, F.; Tassoni, C.; Capolino, G.A. Advances in Diagnostic Techniques for Induction Machines. *IEEE Trans. Ind. Electron.* **2009**, *55*, 4109–4126. [CrossRef]
15. Gao, C.; Nie, Y.; Si, J.; Fu, Z.; Feng, H. Mode Recognition and Fault Positioning of Permanent Magnet Demagnetization for PMSM. *Energies* **2019**, *12*, 1644. [CrossRef]
16. Moon, S.; Jeong, H.; Lee, H.; Kim, S.W. Detection and Classification of Demagnetization and Interturn Short fault of IPMSMs. *IEEE Trans. Ind. Electron.* **2017**, *64*, 9433–9441. [CrossRef]
17. Krichen, M.; Elbouchikhi, E.; Benhadj, N.; Chaieb, M.; Benbouzid, M.; Neji, R. Motor Current Signature Analysis-Based Permanent Magnet Synchronous Motor Demagnetization Characterization and Detection. *Machines* **2020**, *8*, 35. [CrossRef]
18. Ishikawa, T.; Igarashi, N. Failure Diagnosis of Demagnetization in Interior Permanent Magnet Synchronous Motors Using Vibration Characteristics. *Appl. Sci.* **2019**, *9*, 3111. [CrossRef]
19. Faiz, J.; Mazaheri-Tehrani, E. Demagnetization Modeling and Fault Diagnosing Techniques in Permanent Magnet Machines Under Stationary and Nonstationary Conditions: An Overview. *IEEE Trans. Ind. Appl.* **2017**, *53*, 2772–2785.
20. Faiz, J.; Nejadi-Koti, H. Demagnetization Fault Indexes in Permanent Magnet Synchronous Motors—An Overview. *IEEE Trans. Magn.* **2016**, *52*, 8201511. [CrossRef]

Disclaimer/Publisher's Note: The statements, opinions and data contained in all publications are solely those of the individual author(s) and contributor(s) and not of MDPI and/or the editor(s). MDPI and/or the editor(s) disclaim responsibility for any injury to people or property resulting from any ideas, methods, instructions or products referred to in the content.